Domain Structures in Epitaxial Ferroelectric Thin Films

By: Brian Smith

S1711377

Supervised by: Prof. dr. Beatrix Noheda

February 2009

TABLE OF CONTENTS

Introduction

Ferroelectric materials play an essential role in modern technology. Applications of thin film ferroelectrics include nonvolatile memories, microelectronics, electro-optics, and electromechanical systems [1]. Development of ferroelectric thin films began in the late 1960's for use as nonvolatile memories. Despite the promise of these thin films, research was stifled by difficulties processing and integrated ferroelectric films. As a result little progress was made until the 1980's [2]. At this time improvements in processing of thin film ferroelectric oxides allowed high quality films to be grown for research and applications.

The properties of a ferroelectric film depend greatly on the structure of the domains in the film. The domain structure will have a great impact on the dielectric, piezoelectric and optical properties of the film [2]. In order to obtain the optimal properties for specific applications it is necessary to control the domain structure in the film. Different applications of ferroelectric thin films take advantage of different properties of the film. As a result the desired domain structures will vary depending on the application. For example, ferroelectric films used in nonvolatile memories need to have high remnant polarization which is achieved by domains with out of plane polarization. Conversely, domains with polarization in the plane of the film are desired for use as capacitor devices where this domain structure increases the dielectric constant of the film [1].

Controlling the domain structure of epitaxial ferroelectric thin films is vital if such films are to continue to play an important role in practical applications. This paper will examine how different parameters during film growth influence the domain structure in ferroelectric thin films as well as determine what aspects future research must address to continue to make meaningful progress.

1. Background

A ferroelectric crystal is characterized by having a spontaneous polarization in the absence of an electric field below a transition temperature T_c. The spontaneous polarization is the result of a shift in the centrosymmetric position of the atoms in unit cell of the crystal. The atomic shift is very small, on the order of 0.1 Å and is usually coupled with an elongation of the unit cell along the polar axis of the crystal [3].

The spontaneous polarization of a ferroelectric crystal in the absence of an electric field is be oriented in various directions. Regions of the crystal in which the spontaneous polarization are oriented in the same direction are known as ferroelectric domains. Different domains are separated by domain walls [1]. Domain walls are characterized by the approximate angle by which the polarization rotates between the two domains [2]. In epitaxial ferroelectric thin films 180° and 90° domain walls are present. For 90° domain walls the rotation of the polarization must be accompanied by a rotation in the strain, or elongation, across the wall [3]. As a result the 90° domain wall is ferroelectric and ferroelastic. A 180° domain does not have a rotation of the strain across the wall and is only ferroelectric in character [3].

For a tetragonal ferroelectric film on a cubic substrate three different domain structures are possible. A domain in which the c axis of the tetragonal film is aligned normal to the film/substrate interface is known as a *c* domain [4]. Similarly a domain in which the c axis of the tetragonal film is aligned parallel to the film/substrate interface is known as an *a* domain [4]. An *a* domain can have two different orientations a_1 or a_2, the difference being one is rotated 90° from the other [1]. The three domain orientations for a tetragonal film on a cubic lattice are schematically depicted in Figure 1 [4].

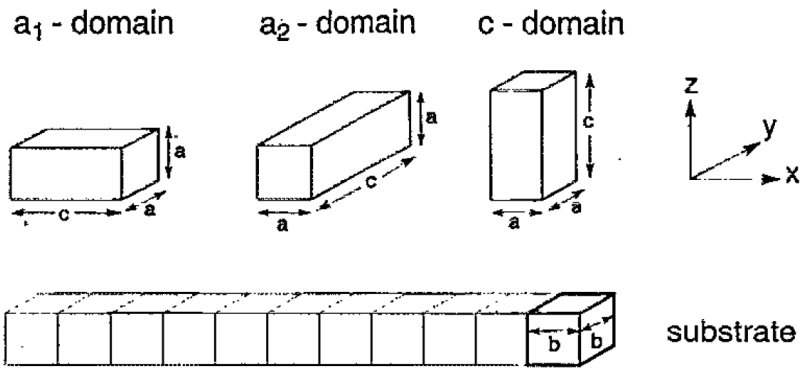

Figure 1. Domain orientations of an epitaxial tetragonal ferroelectric with lattice constants a and c on the [001] face of a cubic substrate with lattice constant b. [4]

The difference between an epitaxial film and a free film is that the former is strained so the lattice parameter of the film matches the lattice parameter of substrate. A free film, on the other hand, is not strained [2]. Coherency is maintained between the film and substrate at the expense of strain in the film. This strain is known as misfit strain [1]. In addition to misfit strain there are two more sources of strain; thermal strain and transformational strain. Thermal strain is caused by the substrate and film having different thermal expansions coefficients. Ferroelectric films are grown at high temperatures above T_c. As the film cools the film and substrate contract by different amounts, creating strain in the film [5]. Transformational strain occurs when the film is cooled below T_c. At this point the elongation of the unit cell occurs adding additional strain in the film [5].

Domain structures occur to minimize the strain and electrostatic energy of the film [4]. Strain in the film can be relaxed by the formation of 90° ferroelastic domains. Since 180° domain walls are not ferroelastic, strain relaxation cannot take place in this way [1]. In addition to domain formation, strain relaxation can occur by the formation of misfit dislocation. This mechanism is especially important above the transition temperature where domains cannot form [6].

2. Experimental Results

The domain structure of an epitaxial ferroelectric film is determined by the conditions in which the film is grown. There are several methods for growing ferroelectric thin films. The two most common techniques are pulsed laser deposition (PLD) and molecular beam epitaxy (MBE) [1]. Although each growth technique has different control parameters, there are several parameters common to all growth techniques which determine the domain structure of the film. This paper will examine the effect of substrate choice, film thickness, and cooling rate on the domain structure.

2.1 Substrate Study

There are many substrates available for epitaxial growth of thin film ferroelectrics. The ferroelectric domain structures of $PbTiO_3$ have been investigated extensively on MgO, $SrTiO_3$, and $KTaO_3$ [5] [7] [8] [9]. The different cubic lattice constants of the substrates result in a different misfit strain in the film. These strains range from large tensile (MgO) to small tensile ($KTaO_3$) to small compressive ($SrTiO_3$) strain. Examination of similar films grown on each substrate provides information about the lattice misfit strain in the film influences the domain structure. Table 1 summarizes the structural parameters of the film and different substrates [5].

Material	Crystal Structure	Lattice Constant (Å)	Misfit Strain ($x10^{-2}$)	Thermal Expansion Coefficient ($x10^{-6}$/K)
$PbTiO_3$	Tetragonal	c= 4.153, a= 3.9775	NA	12.6
MgO	Cubic	a= 4.2551	6.524	14.8
$SrTiO_3$	Cubic	a= 3.9358	-1.05	11.7
$KTaO_3$	Cubic	a= 4.0069	.735	6.67

Table 1. Structural parameters, thermal expansion coefficients and misfit strain of various materials at the growth temperature [5]

In situ synchrotron analysis has been performed on 200 nm thick $PbTiO_3$ films grown on MgO, $SrTiO_3$, and $KTaO_3$ by pulsed laser deposition. The X-ray diffraction (XRD) data was used to determine the *c* domain abundance (α) of the different films [5].

The XRD analysis revealed that the domain structure of $PbTiO_3$ on MgO consists of a predominantly *c* domain structure (α~75%). Cross sectional TEM of the film, Figure 2a, confirms that the domain structure is made up of a large percentage of *c* domains with small *a* domains [5]. $PbTiO_3$ films grown on $SrTiO_3$ produced uniform *c* domains (α=100%). The lack of *a* domains is seen in the TEM image, Figure 2b [5]. The most complicated domain structure was observed on $PbTiO_3$ films on $KTaO_3$. XRD analysis reveals that the film consists of mostly *a* domains (α~30%). Cross sectional TEM, Figure 2c [5], shows thin *c* domains within an *a* domain matrix. However, plane-view TEM, Figure 2d [5], reveals a more interesting domain structure. The *a* domain regions are not uniform but consist of alternating a_1 and a_2 domains. The a/c and a1/a2 domain walls can be differentiated by the direction in which they lie.

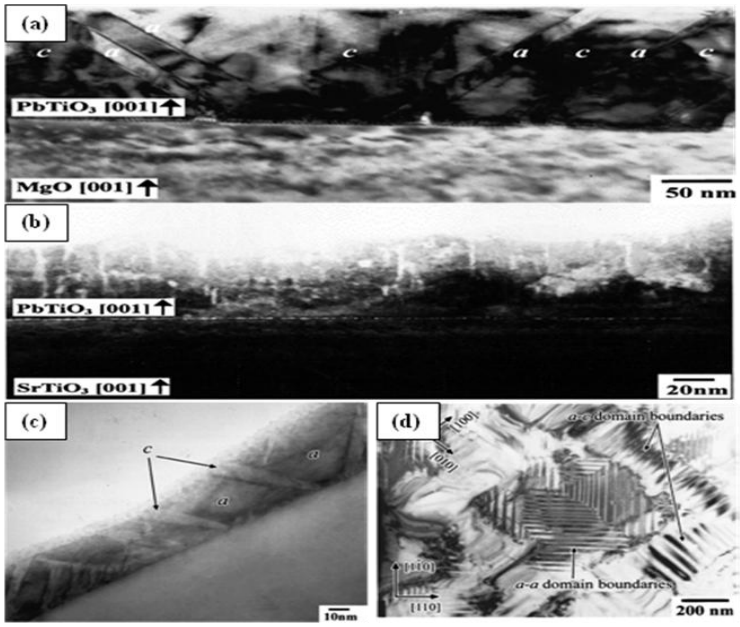

Figure 2. Cross-sectional TEM image of the $PbTiO_3$ films grown on the (a) MgO substrate. (b)$SrTiO_3$ substrate (c) $KtaO_3$ substrate, and (d) Plane-view TEM image of epitaxial $PbTiO_3$ on the $KTaO_3$ [5]

The domain structure in each film can be qualitatively explained by examining the misfit strain and the thermal strain in the film. Adding the thermal strain from cooling at the growth temperature (T_g) to T_c and the misfit strain gives the net strain in the film at T_c. It is important to account for the thermal strain. Although MgO has a larger misfit strain than $KTaO_3$, a film grown on the latter substrate has a larger net strain at Tc due to the large difference in the thermal expansion coefficient between the film and substrate [5]. A plot of α versus net strain is shown in Figure 3 [5]. It is clearly seen from this figure that α is inversely related to the net strain.

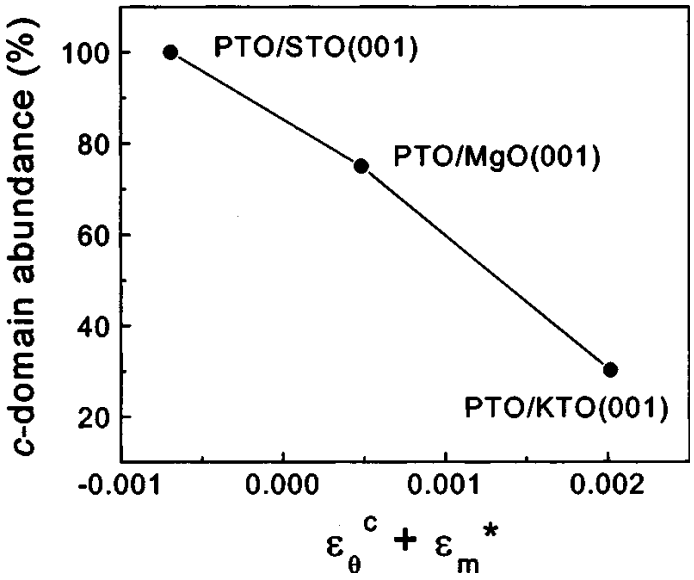

Figure 3. Variation of c-domain abundance as a function of net elastic strain stored in the film [Lee 2001]

To fully grasp how the strain effects the domain structure it is useful to consider three cases; when the substrate is causing a large compressive strain, a large tensile strain, and an intermediate situation where there is only a weak compressive or tensile strain. In the first case, large compressive strain, the film grows *c* domains which minimize the stress since this domain has the smaller lattice parameter. The opposite is true when there is a large tensile strain. The film grows *a* domains where the longer lattice parameter is in the plane of the film. The result is an alternating a_1/a_2 domain structure. In the intermediate case some of the

misfit strain can be relaxed by incorporating a small amount of the *a* or *c* domain in a large amount of the other domain.

Film Thickness Study

Film thickness is another critical parameter that determines the domain structure in ferroelectric films. As mentioned previously, above Tc strain can be partially relaxed by the formation of misfit dislocations. The amount of misfit dislocations present in a given film is directly controlled by the thickness of the film. As the thickness of the film increases the strain required to maintain coherency with the film increases linearly. At a critical thickness the strain energy exceeds the energy required to create a misfit dislocations and the film partially relaxes [4].

To fully explore the effect of film thickness on the domain structure it is important to consider two cases, when the film is subjected to tensile strain from the substrate and when it is under compression. Examination of $PbTiO_3$ films grown on MgO and $SrTiO_3$ provides the tensile and compressive strains respectively.

The α dependence on film thickness for $PbTiO_3$ on MgO films ranging in thickness from 15 to 250 nm is shown in Figure 4 [8]. Initially α increases rapidly with the thickness before saturating at α~75% . This saturation occurs at around a thickness of 100nm.

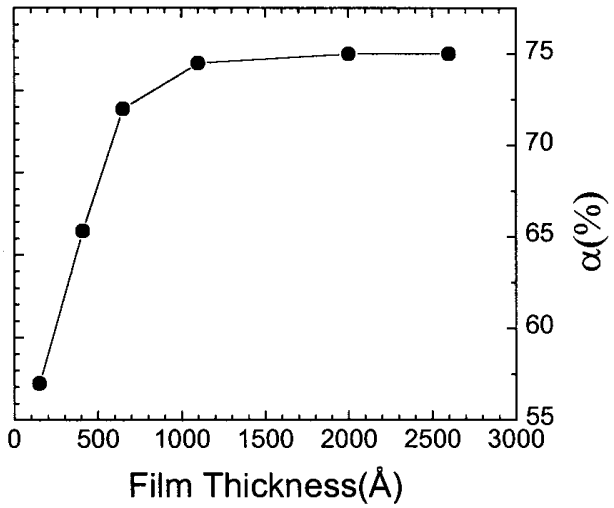

Figure 4. Variation of c-domain abundance as a function of film thickness for $PbTiO_3$ on MgO [Lee 2000]

The change in α with thickness can be explained by examining how the strain in the film evolves with thickness. The dependence of the strain on film thickness is shown in Figure 5 for three substrates [5]. The qualitative behavior for all substrates is the same; the film undergoes a large amount of relaxation as the film thickness initially increases before saturating at a given value. This is also the same qualitative behavior for α as a function of thickness. Since the strain is partially relaxed by misfit dislocations for thick films, a smaller amount of *a* domains are needed to fully relax the film.

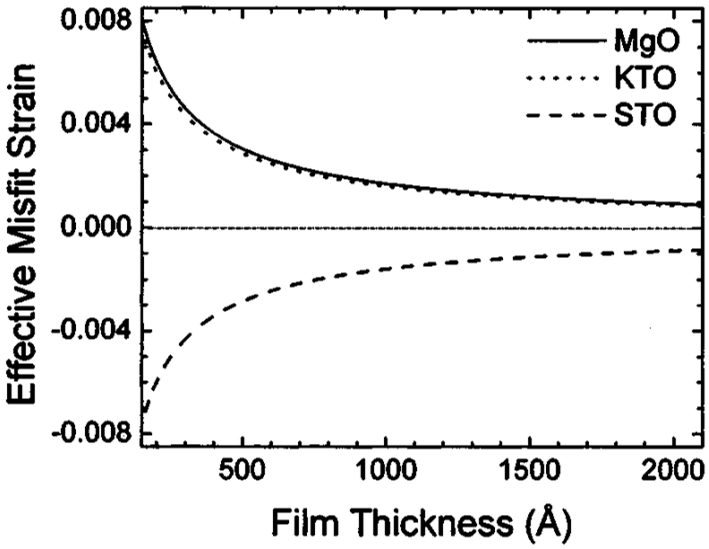

Figure 5. Effective misfit strain as a function of film thickness for epitaxialPbTiO3 thin films grown on MgO, KTaO3, and SrTiO3 [Lee 2001]

The thickness dependence of ferroelectric domains under compressive strain was investigated by varying the thickenss of a $PbTiO_3$ film from 39 to 350 nm on a $SrTiO_3$ substrate. The results of this study are displayed in Figure 6 [10]. The *a* domain abundance dropes to zero for films thinner than 39 nm. Increasing the thickness results in an increase in the *a* domain abundance. This increase begins to taper off for films thicker than 350 nm. This thickness dependence is qualitatively opposite to what is observed for the tensile case, $PbTiO_3$ films on MgO. This is expected since the sign of the strain is also opposite. So, for this film, it is the *c* domain that provides strain relaxation and there will be less strain to relax for thicker films.

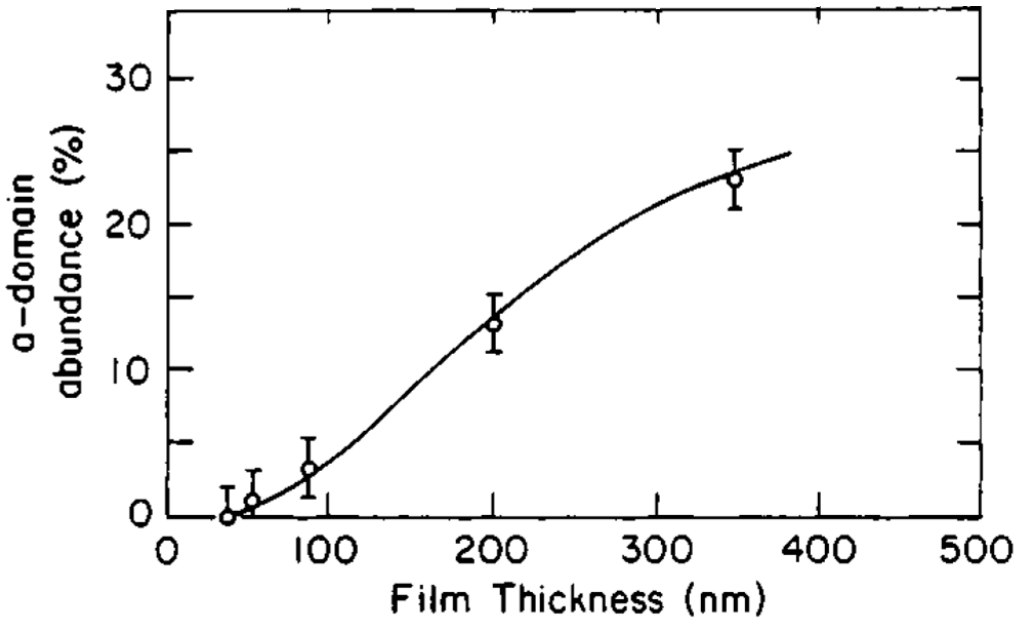

Figure 6. The change in the *a* domain abundance with film thickness. [Hsu]

With advances in thin film deposition of ferroelectric it is now possible to synthesize high quality ferroelectric films with thicknesses less than 100 nm known as ultrathin films. For many ferroelectric films this is below the critical thickness for misfit dislocation generation. However, even in this regime the thickness still plays an important role in determining the domain structure. A known law for ferroelectric domains states that the

width of the domains is directly proportional to the square root of the thickness. This law, known as Roytburd's Law [11], has been shown to hold true for increasingly thin ferroelectric film but is there a critical thickness below which this law breaks down? With the ability to examine ultra thin films it is now possible to study this question experimentally. To fully address this question both 90° and 180° domain structures will be examined to determine if, when, and why Roytburd's Law breaks down.

To examine the behavior of 90° domain structures in ultrathin films of 30 nm $PbTiO_3$ films were grown on $DyScO_3$ substrates. At the growth temperature there is a very good lattice mismatch between the film and the substrate which prevents misfit dislocations from forming [4]. At room temperature the film is sufficiently strained to produce a 90° domain pattern. The resulting XRD and TEM analysis, the latter shown in Figure 7a [12], clearly show the 90° domain pattern made up of alternating *a/c* domains. The domain periodicity was found to be 27 nm. What was interesting about the TEM image is the uniformity of the *a* domains widths; approximately 6-7nm.

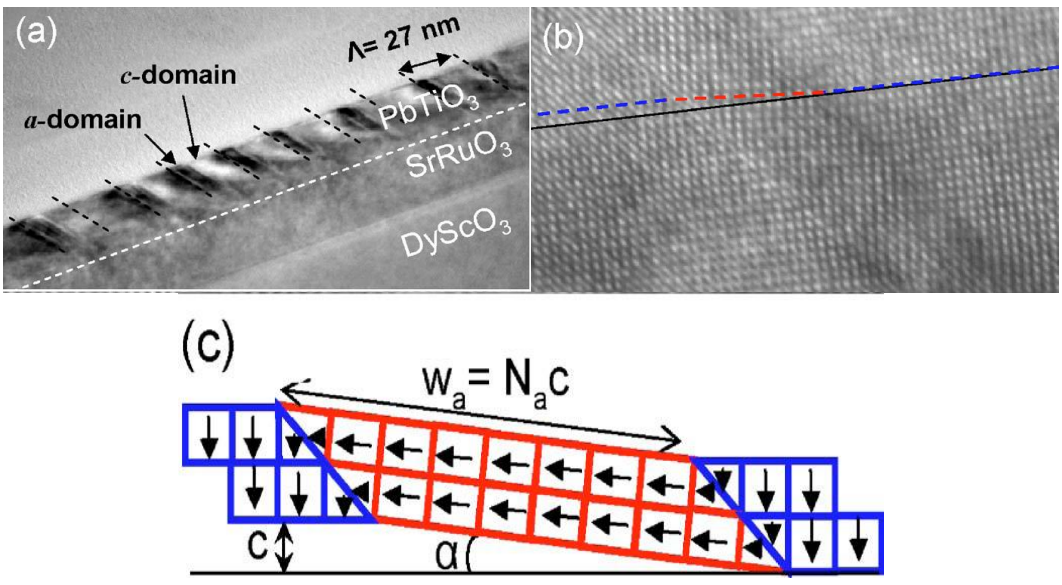

Figure 7. (a) TEM image of a 30 nm thick film of $PbTiO_3$ with a $SrRuO_3$ buffer layer on DyScO3. The dashed lines indicate the wall positions. (b) TEM image around an *a*-domain band. The dashed lines show the coherent connection between two c domains mediated by the narrow *a* domain. (c) A sketch of the c/a/c chain. [12]

To understand why this occurs as well as determine a critical thickness for Roytburd's Law it is important to understand the origin of 90° domain walls. In order for the film to create a 90° domain wall twinning, must occur in which the body diagonal of a unit cell on the domain wall is shared by each domain [12]. As seen in the high resolution TEM in Figure 7b and schematically in Figure 7c [12], twining introduces a small deviation from the 90° rotation of the polarization. The deviation is defined by the tilt angle α. As a result of tilt angle the *a* domains cannot have any arbitrary width. The widths of the *a* domains have to be appropriately sized so that direction of polarization of neighboring *c* domains remains coherent. This introduces a minimum possible width of the *a* domains defined as $w_a^{min}=c/\sin(\alpha)$. For $PbTiO_3$, w_a^{min} ~6.2 nm [12]. As a result, the domain periodicity observed is the smallest possible for a 90° domain structure in a $PbTiO_3$ film representing a critical thickness below which Roytburd's Law no longer applies.

Twinning does not occur in 180° domains, so the critical thickness where Roytburd's Law breaks down is not limited in the same way as 90° domains. To examine the periodicity of 180° domains a series of $PbTiO_3$ films were grown on $SrTiO_3$ with thicknesses ranging from 42 nm-1.6 nm [13]. The compressive epitaxial strain results in the films having pure *c* domain with a 180° domain structure. The stripe period as a function of film thickness is shown in Figure 8 [13]. The experimental results are shown by the open and closed circles while the solid line represents the predicted stripe period using Roytburd's Law. The difference between the two sets of experimental data points is that the open circles (F_α) represent the high temperature domain period and the closed circles (F_β) are the lower temperature domain period. There is a good agreement between experiment and theory all the way to the smallest film; 1.6nm.

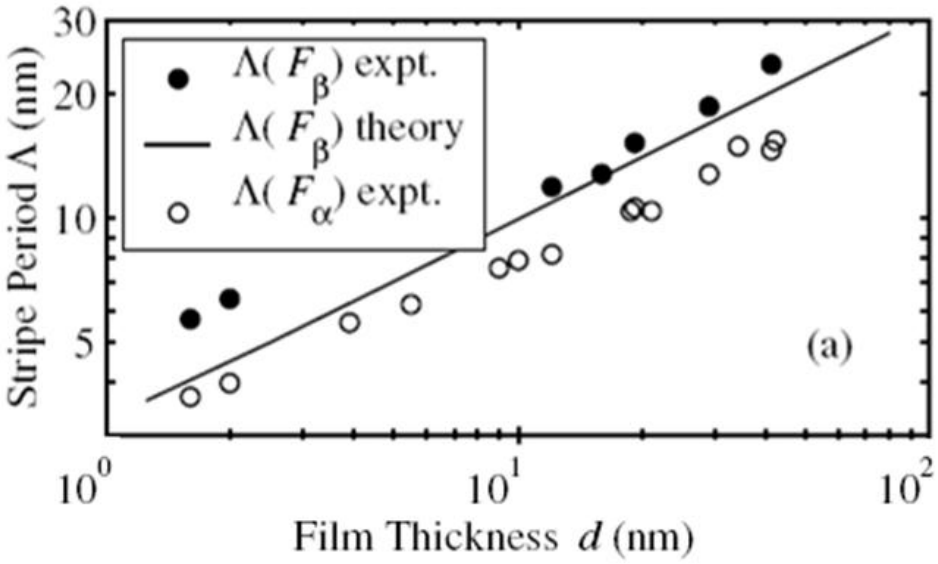

Figure 8. Stripe period vs. thickness, circles represent experiment the solid line represents theory. [13]

It is clear that Roytburd's Law holds for 180° domain in even extremely thin films. Experimentally the critical thickness where this law breaks down has not been reached. As a result, this limit must be explored theoretically and will be shown later.

Cooling Rate

Changing the substrate or the film thickness influences the domain structure through the strain in the film. These two growth parameters influence a single property of the film, the strain. There are, however, other parameters that influence the domain structure without changing the strain in the film. One such parameter is the cooling rate after film deposition.

To investigate the effect of the cooling rate on the 90° domain structure in 400 nm $PbTiO_3$ films were grown on $SrTiO_3$. These films were then subjected to three cooling rates; slow cooling (~5°C/min), normal cooling (~30°C/min) and fast cooling (~100°C/min). Slow and normal cooling was achieved by control of a heater attached to the substrate. For fast cooling the sample was removed from the heater after growth and allowed to cool freely, as a result this cooling rate is estimated [14].

The domain structures were analyzed using XRD to determine the volume fraction of *a* domains in each sample. As the cooling rate increased, the volume fraction of the *a* domains decreased. The volume fraction of the *a* domains for each sample is as follows; slow cooling 15%, normal cooling 13.4%, and fast cooling 6.7% [14]. Two kinetic processes are considered to be the cause of the domain structure dependence on the cooling rate. These two processes are the domain nucleation and domain wall motion [14]. The paraelectric to ferroelectric phase transition which is responsible for the creation of domain structures is a nucleation limited process [14]. Therefore, increasing the cooling rate through this transition limits nucleation. This causes a smaller fraction of *a* domains to form in films cooled rapidly.

However, even with limited nucleation the films should still be able to relax to the same fraction of *a* domains below the phase transitions, regardless of the cooling rate [1]. Apparently this is not the case. The mobility of the 90° domain walls must be impeded by faster cooling preventing the growth of *a* domains to fully relax the film [1]. The precise influence of these two effects on the domain structure remains unknown. *In situ* XRD analysis of films subjected to different cooling rate would be useful in analyzing the kinetics of 90° domain wall motion.

3. Theoretical Predictions

3.1 Phenomenological models

A theoretical model to predict domain structures in ferroelectric film was created by Roytburd in the mid 1970's [1]. This theory used a mean strain approach in involving a summation of elastic energy and domain boundary energy. The equilibrium configurations were determined by minimizing the summation [11]. While being relatively simple mathematically, this theory provides a good quantitative description of domain structures in most circumstances. The result of this theory was to predict the fraction of c domains as a function of misfit strain and film thickness [11]. This analysis also leads to the square root dependence of the domain period on the film thickness, Roytburd's Law which was discussed earlier.

Although this theory was found to provide good predictions for the domain structure there were a number of important factors not taken into account. This theory did not address strain relaxation from misfit dislocations. To incorporate misfit dislocations, an effective substrate lattice parameter was introduced. This parameter changed the misfit strain in the film used in the theory to accurately reflect strain relaxation that occurred from misfit dislocation [6].

Even using an effective substrate lattice parameter the theory still does not accurately predict the domain structure of the film under certain circumstances. For example, for a film subjected to appropriate tensile strain the theory predicts that below a critical thickness a mono-*a* domain structure will occur. However, it was found that an a_1/a_2 domain structure was always formed [15].

Another theoretical approach has been developed using a Landau-Ginzburg-Devonshire theory (16). In this theory the free energy of the system is expanded in terms of an order parameter. For ferroelectric thin films, the polarization is often used as the order parameter. The free energy as an expression of the order parameter is then minimized to determine the equilibrium domain structure. This theory has been found to produce an improvement over the mean strain approach but still does not correctly predict the domain structure under certain circumstances [1].

3.2 First Principles: Models

First principles modeling is another theoretical approach for analyzing domain structures in ferroelectric thin films. This approach has many advantages over the previously discussed phenomenological models. There is no need for any empirical parameters or other assumptions. Empirical parameters needed for phenomenological theories have a tremendous impact on the results [17] and can be difficult to determine [18]. First principle calculations allow researchers a great degree of freedom choosing what conditions the theoretical film will be subjected to. As a result, it is possible to isolate and examine different factors affecting the domain structure such as strain, size effects, external electric fields, and surfaces/interfaces [19]. First principle calculations not only have advantages over other theoretical approaches but also over experimental studies. It has been shown that thin film synthesis can have a great impact on the properties of the film [20]. First principle calculations eliminate this effect and study only the intrinsic properties of the film.

The major disadvantage of first principle calculations is the limitation of the system size that can be reasonably analyzed. Initially this shortcoming prevented the use of this method for studying ferroelectric thin films. However, with advances in algorithms and computing, increasing large and complex system are able to be simulated which eventually

enabled first principle calculations to become a viable method to analyze ferroelectric thin films [19]. It is possible to study systems of increasing size and complexity by creating non-empirical models using parameters determined from fitting selected first principle calculations. The size of the films that can be studied with first principle models is still smaller than films used for technological applications. However, improvements in ultra thin film synthesis allow a direct comparison between first principle results and experimental observations making first principle models a valuable tool for studying ferroelectric thin films.

The geometry used to study thin films with first principle models is a single crystalline planar slab. First principle models require three dimensional periodicity, so the slab is repeated periodically to produce a supercell [19]. To model a specific film, several variables need to be defined. These variables include the orientation, number of atomic layers, and choice of termination of the interfaces [19]. The direction of polarization is determined by the initial structure. An epitaxial film is simulated by fixing the in-plane lattice parameters of the film to the bulk lattice parameters of the desired substrate [21].

First principle modeling can take two forms; parameterized interatomic potentials and effective Hamiltonians [19]. This paper will explore the construction of an effective Hamiltonian to provide further insight in to how first principle modeling works and explore the usefulness of such model. To begin, the effective Hamiltonian will be a function of two quantities; the local soft mode and the strain variables [22]. Later more variables will be added to increase the complexity and realism of the model system.

The soft mode characterizes a lattice vibration where the frequency becomes zero upon cooling through a phase transition [23]. The vanishing frequency of this lattice vibration corresponds to a vanishing restoring force against the deformation caused by the vibration.

When the frequency of this vibration becomes zero there is no restoring force and an atomic displacement occurs. For $PbTiO_3$ the soft mode involves the Pb^{2+} and Ti^{4+}cations moving along the [001] direction and the oxygen anions moving in the opposite direction [23]. At the phase transition this frequency of this vibration mode becomes zero causing a displacement of these ions from their centrosymmetric positions resulting in a spontaneous polarization along the [001] direction. A schematic of the behavior of a soft mode is displayed in Figure 9 [23].

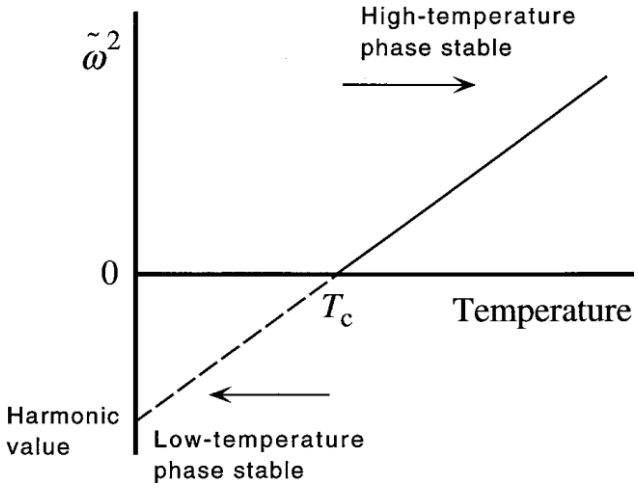

Figure 9. Schematic representation of the behavior of the soft mode. [23]

The soft mode can be described as collective motion of local modes or more specifically as a linear superposition of local modes having the same amplitude in each unit cell [22]. However, there is more than one possible choice of local modes to describe a soft mode. To simplify the effective Hamiltonian, the local modes should be as symmetric as possible to minimize the number of expansion terms in the equation [22]. Interactions between local modes are harder to evaluate than the self energy of a local mode, so the chosen local modes should minimize the number of interactions. For an ABO_3 film these simplifications are achieved by centering the local modes on atom A or B [22]. In this formalism the local mode amplitude for a given unit cell *i* is denoted $\mathbf{u}_i$.

The strain variables define the elastic deformation in the film. There are two components to the total strain; homogeneous and inhomogeneous strain. The homogeneous strain is the strain applied uniformly to each unit cell [22]. The effective Hamiltonian is not a function of this type of strain. Inhomogeneous strain represents the strain of each individual unit cell. There are six strain variables per unit cell. These six variables are not independent and can be represented by three dimensionless displacements, $\mathbf{v}_i$ [22]. It is these dimensionless displacements which are varied when simulating the effective Hamiltonian.

To minimize the computational requirements of the model, two basic approximations are made constructing the effective Hamiltonian. The first approximation is that the effective Hamiltonian can be represented as a low order Taylor series [24]. Ferroelectric phase transitions involve only very small atomic displacements and strain deformations. As a result, the atomic configurations that are the most significant will be those close to the cubic structure. So, the energy of the film can be described as a Taylor expansion of the displacement from the cubic structure. Four terms of this expansion are needed since ferroelectricity is an anharmonic phenomenon [24]. Higher order terms can be included to refine the model at the expense of additional computation.

The second approximation provides the reason for the effective Hamiltonian being a function of only the soft mode and the strain. A ferroelectric phase transition is characterized by a decrease in the frequency of the soft mode to zero and the appearance of strain. All other lattice vibrations are hardly affected by the transition. Describing the energy of the system using only the soft mode and strain decreases the degrees of vibration freedom from 15 to 6, significantly simplifying the calculations [22].

To describe the energy of the system the effective Hamiltonian consists of five parts; a local mode self energy, a long range dipole-dipole interaction, short range interactions

between soft modes, an elastic energy, and an interaction between local modes and local strain. The overall equation for the total effective Hamiltonian is given in Equation 1 [22]. Each energy component in this equation will be explored below.

$$E^{\text{tot}} = E^{\text{self}}(\{\mathbf{u}\}) + E^{\text{dpl}}(\{\mathbf{u}\}) + E^{\text{short}}(\{\mathbf{u}\}) + E^{\text{elas}}(\{\eta_l\}) + E^{\text{int}}(\{\mathbf{u}\},\{\eta_l\}) , \quad (1)$$

$$E(\mathbf{u}_i) = \kappa_2 u_i^2 + \alpha u_i^4 + \gamma(u_{ix}^2 u_{iy}^2 + u_{iy}^2 u_{iz}^2 + u_{iz}^2 u_{ix}^2) \quad (2)$$

$$E^{\text{self}}(\{\mathbf{u}\}) = \sum_i E(\mathbf{u}_i) \quad (3)$$

$$E^{\text{dpl}}(\{\mathbf{u}\}) = \frac{Z^{*2}}{\epsilon_\infty} \sum_{i<j} \frac{\mathbf{u}_i \cdot \mathbf{u}_j - 3(\hat{\mathbf{R}}_{ij} \cdot \mathbf{u}_i)(\hat{\mathbf{R}}_{ij} \cdot \mathbf{u}_j)}{R_{ij}^3} \quad (4)$$

$$E^{\text{short}}(\{\mathbf{u}\}) = \frac{1}{2} \sum_{i \neq j} \sum_{\alpha\beta} J_{ij,\alpha\beta} u_{i\alpha} u_{j\beta} \quad (5)$$

$$\text{first NN}: \quad J_{ij,\alpha\beta} = (j_1 + (j_2 - j_1)|\hat{R}_{ij,\alpha}|)\delta_{\alpha\beta} ; \quad (6)$$

$$\text{second NN}: \quad J_{ij,\alpha\beta} = (j_4 + \sqrt{2}(j_3 - j_4)|\hat{R}_{ij,\alpha}|)\delta_{\alpha\beta} + 2j_5 \hat{R}_{ij,\alpha}\hat{R}_{ij,\beta}(1 - \delta_{\alpha\beta}) ; \quad (7)$$

$$\text{third NN}: \quad J_{ij,\alpha\beta} = j_6\delta_{\alpha\beta} + 3j_7 \hat{R}_{ij,\alpha}\hat{R}_{ij,\beta}(1 - \delta_{\alpha\beta}) \quad (8)$$

$$E^{\text{elas}}(\{\eta_l\}) = E_I^{\text{elas}}(\{\eta_{I,l}\}) + E_H^{\text{elas}}(\{\eta_{H,l}\}) , \quad (9)$$

$$E_H^{\text{elas}}(\{\eta_{H,l}\}) = \frac{N}{2} B_{11}(\eta_{H,1}^2 + \eta_{H,2}^2 + \eta_{H,3}^2) + N B_{12}(\eta_{H,1}\eta_{H,2} + \eta_{H,2}\eta_{H,3} + \eta_{H,3}\eta_{H,1}) + \frac{N}{2} B_{44}(\eta_{H,4}^2 + \eta_{H,5}^2 + \eta_{H,6}^2). \quad (10)$$

$$E_I^{\text{elas}} = \sum_i \Big\{ \gamma_{11}[v_x(\mathbf{R}_i) - v_x(\mathbf{R}_i \pm \mathbf{x})]^2 + \gamma_{12}[v_x(\mathbf{R}_i) - v_x(\mathbf{R}_i \pm \mathbf{x})][v_y(\mathbf{R}_i) - v_y(\mathbf{R}_i \pm \mathbf{y})] + \gamma_{44}[v_x(\mathbf{R}_i) - v_x(\mathbf{R}_i \pm \mathbf{y}) + v_y(\mathbf{R}_i) - v_y(\mathbf{R}_i \pm \mathbf{x})]^2 + \text{ cyclic permutations} \Big\} , \quad (11)$$

$$E^{\text{int}}(\{\mathbf{u}\},\{\eta_l\}) = \frac{1}{2} \sum_i \sum_{l\alpha\beta} B_{l\alpha\beta} \eta_l(\mathbf{R}_i) u_\alpha(\mathbf{R}_i) u_\beta(\mathbf{R}_i) \quad (12)$$

The equation for the local mode self energy is shown in Equation 2 [22]. Where $E(\mathbf{u}_i)$ is the energy of an isolated self mode at unit cell $\mathbf{R}_i$ with an amplitude $\mathbf{u}_i$ compared to that of the perfect crystal structure [22]. This term is summed over all the unit cells to obtain the total self energy. To describe the ferroelectric film $E(\mathbf{u}_i)$ must include harmonic and anhormic terms. The cubic reference structure prevents any odd terms from entering into the equation for $E(\mathbf{u}_i)$, which is shown in Equation 3 [22]. This equation contains three expansion parameters $\kappa 2$, α, and γ which need to be calculated from first principles.

The equation for the long range dipole-dipole interactions in atomic units is shown in Equation 4 [22], where is Z^* the Born effective charge for the soft mode and ε_∞ is the optical dielectric constant of the film. This interaction is the only long range interaction between local modes. The dipole moment associated with local mode *i* is expressed by $\mathbf{d}_i = Z^* \cdot \mathbf{u}_i$ [21].

Short range interactions between soft modes are the result of differences of short range repulsions and electronic hybridization between two adjacent local modes and that of two isolated local modes. The equation for this energy contribution expanded to the second order is displayed in Equation 5 [22]. The term $J_{ij\alpha\beta}$ is the coupling matrix between neighboring local modes *i* and *j*. Since these are short range interactions $J_{ij\alpha\beta}$ will decrease very rapidly for an increase in R_{ij}. The coupling matrix can be determined for any arbitrary number of nearest neighbors. In this example the short range interactions between three degrees of nearest neighbors are considered. The equation between the coupling matrixes of nearest, next nearest, and next next nearest neighbors are shown in Equations 6, 7, and 8 respectively [22]. The coefficients j1,…,j7 are the intersite interactions which can be seen schematically in Figure 10 [22].

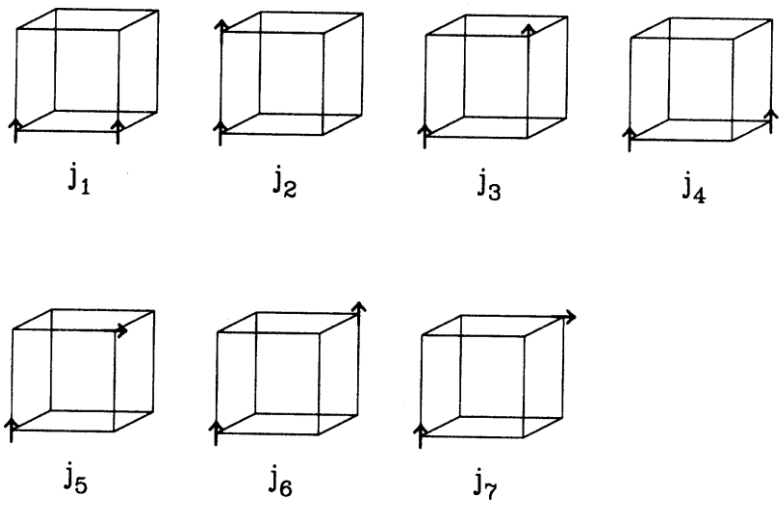

Figure 10. The independent intersite interaction coefficients. [22]

The elastic energy term is the sum of two energies, Equation 9 [22]. These two energies represent the energy contribution from the homogeneous strain and the inhomogeneous strain. The homogenous strain tensor is represented by six components η_ℓ, where $\ell=(1,\ldots,6)$ using Voigt notation, see Appendix A. The homogenous strain allows the simulated cell to vary in shape. An epitaxial film is simulated by setting $\eta_1= \eta_2=\delta$ and $\eta_6=0$

where δ represents the misfit strain [22]. The homogeneous elastic energy is shown in Equation 10 [22], where N is the number of unit cells that will be simulated and B is the elastic constant. The inhomogeneous strain represents the local distortions of a given unit cell in terms of the dimensionless displacement variables, $\mathbf{v}_i$, defined earlier. Energy expression for the inhomogeneous strain is displayed in Equation 11 [22]. The three terms in the sum correspond to energy of bond stretching, correlation, and bending, respectively, caused by local deformations.

The last energy contribution to the effective Hamiltonian is shown in Equation 12 [22]. This term describes the interactions between the local modes and the local strain. As indicated by the variable η_ℓ the homogeneous and inhomogeneous strains are both present in this equation. $B_{\ell\alpha\beta}$ is the coupling constant between the strain and the local modes. There are only three independent coupling constants which simplifies this equation.

All the parameters needed to solve the effective Hamiltonian can be calculated using first principles. In this model no empirical input is needed. Exploring how these parameters are calculated using density-functional theory will not be covered in this paper. However, the calculated parameters for a $BaTiO_3$ film are shown in Table 2 [22]. The calculated intersite interaction coefficients ($j_1,\ldots,j_7$) are all very small which means these interactions will decay very quickly with increasing distance. This confirms that these interactions are truly short range. Using these parameters, the ratio of the degrees of nearest neighbor interaction can be calculated to confirm if the choice of using three degrees of interactions was appropriate. The ratio was found to be 1: 0.23 : 0.09, which confirms that further neighbor interactions will only have a very small effect [22].

On-site	κ_2	0.0568	α	0.320	γ	−0.473
Intersite	j_1	−0.02734	j_2	0.04020		
	j_3	0.00927	j_4	−0.00815	j_5	0.00580
	j_6	0.00370	j_7	0.00185		
Elastic	B_{11}	4.64	B_{12}	1.65	B_{44}	1.85
Coupling	B_{1xx}	−2.18	B_{1yy}	−0.20	B_{4yz}	−0.08
Dipole	Z^*	9.956	ϵ_∞	5.24		

Table 2. Expansion parameters for the effective Hamiltonian for $BaTiO_3$, energy is in Hartrees. [22]

Additions to the effective Hamiltonian presented above have been made to increase the versatility of the model. These additions allow more complex and realistic systems to be studied. This paper will examine two additions to the effective Hamiltonian. The first addition will allow for a compositional degree of freedom which can be used to model ferroelectric alloys such as $Pb(Zr_{1-x}Ti_x)O_3$. The second addition will introduce a parameter to control the degree of screening of the depolarizing field to determine the effect of electrical boundary on various systems.

To model an alloy ferroelectric film the effective Hamiltonian must have a compositional degree of freedom. This is done by adding another term to the effective Hamiltonian presented above. This modified effective Hamiltonian is shown in Equation 13 [25]. In this equation E_{ave} is the effective Hamiltonian for the simple ABO_3 system which has already been explained. The second term, E_{loc}, introduces the parameter σ_j which characterizes the atomic configuration of the alloy.

$$E(\{\mathbf{u}_i\},\{\mathbf{v}_i\},\eta_H,\{\sigma_j\}) = E_{\text{ave}}(\{\mathbf{u}_i\},\{\mathbf{v}_i\},\eta_H) + E_{\text{loc}}(\{\mathbf{u}_i\},\{\mathbf{v}_i\},\{\sigma_j\}) \quad (13)$$

$$E_{\text{loc}}(\{\mathbf{u}_i\},\{\mathbf{v}_i\},\{\sigma_j\}) = \sum_i [\Delta\alpha(\sigma_i)u_i^4 + \Delta\gamma(\sigma_i)(u_{ix}^2u_{iy}^2 + u_{iy}^2u_{iz}^2 + u_{iz}^2u_{ix}^2)] + \sum_{ij}[Q_{j,i}(\sigma_j)\mathbf{e}_{ji}\cdot\mathbf{u}_i + R_{j,i}(\sigma_j)\mathbf{f}_{ji}\cdot\mathbf{v}_i], \quad (14)$$

$$E_{H\text{eff}}(\{\mathbf{u}_i\},\{\mathbf{v}_i\},\eta,\{\sigma_i\}) - \sum_i \beta 2\pi \frac{Z^2}{a^3\epsilon_\infty}\langle u_{j,z}\rangle_s u_{i,z}, \quad (15)$$

The expressions for E_{loc} will account for the effect of an alloy on the self energy and the intersite contributions. The functional form of E_{loc} is given in Equation 14 [25]. The first term in this expression characterizes the onsite contribution of the alloy. This expression has the same functional form as the self energy of a non-alloy, the only difference being the coefficients are replaced with $\Delta\alpha(\sigma_j)$ and $\Delta\gamma(\sigma_j)$. These two coefficients take into account the contribution of the alloy.

The second term in Equation 14 represents the intersite contributions. The terms $\mathbf{e}_{ij}$ and $\mathbf{f}_{ij}$ are unit vectors that point from site j to the origin of the local mode, $\mathbf{u}_i$, and displacement, $\mathbf{v}_i$, respectively [25]. Once again the coefficients $R(\sigma_j)$ and $Q(\sigma_j)$ represent the alloy-induced contributions to the intersite energy. The first term in the sum provides a description of the alloy induced local mode intersite interactions. The second term in the sum represents the effect of the alloy on the elastic intersite interactions. Higher order powers of $\mathbf{u}_i$ and $\mathbf{v}_i$ can be included in this equation, but this level of detail has been found to produce a good agreement with experimental results [25]. The compositional parameters are determined from first principle calculations.

The effective Hamiltonian presented thus far only models a ferroelectric film under open circuit conditions [26]. To model films that are not under ideal open circuit conditions an expression is added to the effective Hamiltonian which models the effect of an internal field in the film. This internal field arises to partially or fully screen the polarization induced surface charges. The effective Hamiltonian to model a film under different electrical boundary conditions is shown in Equation 15. [26]

The first term in this equation is the alloy effective Hamiltonian developed above. The second term in the equations accounts for the internal field. The energy of the internal field is a function of the Born effective charge, the lattice constant (a), the dielectric constant, and the average of the z component of the local modes centered at the surfaces $\langle u_{j,z} \rangle_s$. The parameter β is introduced to control the strength of the internal field. An open circuit configuration is achieved by setting β=0. Increasing β will decrease the strength of the field. When β is large enough the energy of the internal field will disappear and the short circuit condition is reached. The value required to reach the ideal short circuit condition will depend on the geometry of the supercell [26].

Solving the effective Hamiltonian is achieved using a Monte Carlo simulation. This approach is used because a Monte Carlo simulation only computes changes in the total energy which reduces the calculations needed for the simulation [22]. During the simulations a single variable is changed and the total energy change is then calculated. If the energy decreases than the move is accepted. In one sweep of the simulation each $\mathbf{u}_i$ is varied in sequence followed by a change in each $\mathbf{v}_i$ in sequence. When one sweep is completed the variable being explored in the particular study is then changed and another sweep is performed. To ensure that the system has reached its lowest possible energy state tens of thousands of sweeps are performed [22].

3.3 First Principles: Thickness Study

A first principle effective Hamiltonian model is a powerful tool to study the domain structures in ultrathin ferroelectric films. This technique has been used to explore if a critical thickness exists below which Roytburd's Law breaks down for 180° domains. This example illustrates the power of using first principle models. The simulated films were $Pb(Zr_{0.4}Pb_{0.6})O_3$ oriented in the [001] direction. These films were simulated to be under a compressive misfit strain of -2.65% at 10 K with 80% screening of the depolarizing field. These conditions were chosen to create 180° domains in the simulated films [21]. To determine the critical thickness for Roytburd's Law films of varying thickness from 1.2 nm to 14.4 nm were simulated. To perform the simulation stripe domain periods alternating along the x direction with a chosen domain period were constructed. These domains were then allowed to relax over a Monte Carlo simulation.

The ground state domain periodicity as a function of the square root of the film thickness is plotted in Figure 11 [21]. Linear fit of the data points for films thicker than 2.0 nm confirm that Roytburd's Law applies for these films. This result is in agreement with the experimental result examined earlier. However, for the thinnest film, 1.2nm thick, no ground state period was found. This means that for films thinner than 1.2nm Roytburd's Law breaks down and the domain periodicity is no longer proportional to the square root of the thickness.

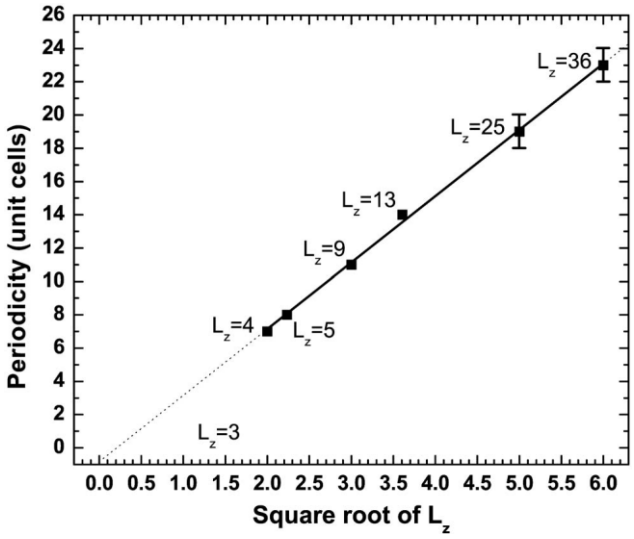

Figure 11. Periodicity as a function of the square root of the thickness-related integer. [21]

In addition to determining the critical thickness for Roytburd's Laws these simulations also provide insight into the morphology of the domains when the film thickness is varied. The total energy per unit cell of the film as a function of the domain period is displayed in Figure 12 [21] for several film thicknesses increasing from left to right. The lowest point on the plot corresponds to the ground state stripe domain periodicity. The other points in the plot represent metastable stripe domain periods. These figures display an interesting trend. The energy curves become smoother as the thickness of the film increases with more metastable periodicities close to the energy of the ground state period. As a result, thicker films should have domains of varying widths. It should be noted that this result has been observed experimentally [13] [27].

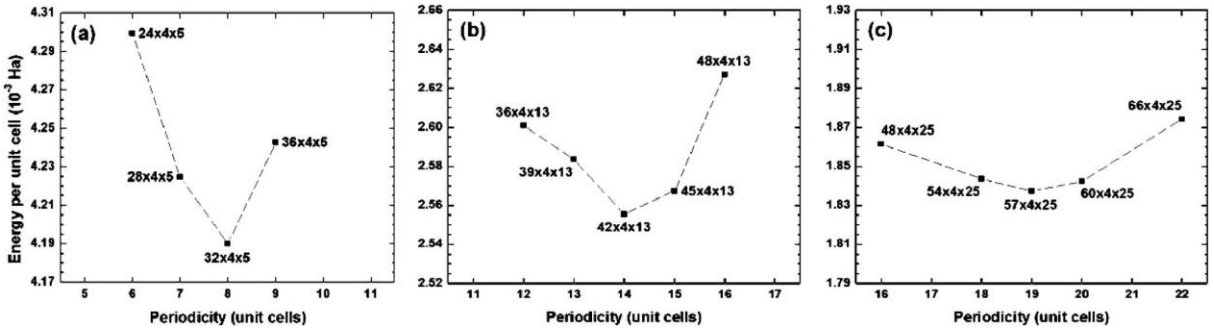

Figure 12. Energy per unit cell as a function of stripe periodicity for (a) 2.0 nm (b) 5.2 nm, and (c) 10.0 nm thick films [21]

Figure 13 [21] shows a cross sectional view of dipole configurations of the ground state stripe periods for three film thicknesses; 14.4 nm, 5.2 nm, and 1.2 nm respectively. For thick films 180° domains occupy the majority of the film. However, near the interfaces 90° domains are present to minimize the depolarizing field [21]. As film thickness decreases the ratio of 180° domains to 90° domains becomes smaller and smaller. Eventually the domain structure of the film resembles a vortex-like structure; Figure 13b [21]. It is interesting that as the 180/90° domain ratio decreases Roytburd's Law still holds and continues to do so even when vortex structures occur. However, this result is not entirely surprising since pure 90° domains also follow Roytburd's Law. Roytburd's Law finally breaks down in the 1.2 nm thick film as a result of the domain structure becoming a monodomain state with polarization in-plane; Figure 13c [21].

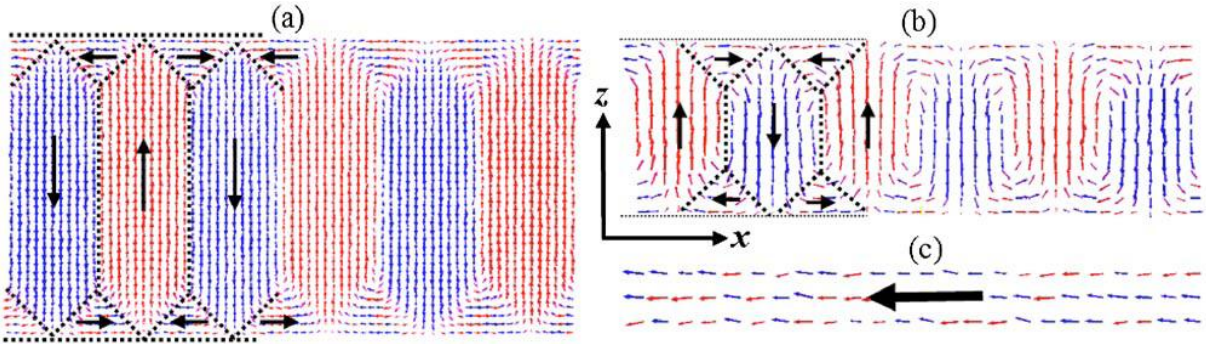

Figure 13. Cross-sectional view of dipole arrangement of stripe domains in (a)14.4 nm, (b) 5.2 nm, and (c) 1.2 nm thick films. The red and blue arrows characterize local dipoles having positive and negative components along the z axis, respectively. The dotted lines represent domain boundaries, while the nominal dipole directions in the domains are indicated by black arrows [21]

4. Future Work

Work on epitaxial ferroelectric thin films has made great progress in devolving a fundamental understanding of the domain structure in these thin films. However, there are still unanswered and half-answered questions that need to be addressed to expand the body of knowledge in this field.

Methods for ferroelectric thin film growth need to be continually improved to allow the synthesis and characterization of thinner films. Also, the size and complexity of model systems that can be studied needs to be expanded. This will create a larger overlap for direct comparison between theoretical simulations and experimental observations. Having direct experimental observations to evaluate theoretical simulations enables theoreticians to refine first principle models. New additions will be made to the effective Hamiltonian to increase the realism of these models to match with experimental observations. In turn, experimentalists will benefit as well. The refinement of first principle models will result in a greater fundamental understanding how specific parameters influence the domain structure of ferroelectric thin films. This fundamental understanding can then be used by experimentalists to improve synthesis techniques to create and study new systems.

Another aspect of this field that is not fully understood is how the kinetics of domain nucleation and growth affect the final domain structure. Experimental observations clearly show that the cooling rate of the film to room temperature from growth temperature has a large impact on the domain structure. Suppression of domain nucleation and obstruction of domain wall motion have been proposed as reasons for the experimental observations. However, the exact influence of each factor on the domain structure remains unclear. *In situ*

observation of kinetic domain processes upon cooling would prove very insightful in examining this question.

There are a number of challenges that first principle modeling must address to analyze more realistic systems. These challenges include the incorporation of defect effects and external electric fields. In addition to these specific challenges for ferroelectric thin films, first principle modeling will benefit greatly from advances in computing which will enable larger systems to be modeled.

Interest in ferroelectric thin films is driven by the potential for creating ferroelectric materials with enhanced material properties for technological applications. This interest must remain high if researchers and funding will continue to be devoted to this field. Therefore, further insight into the fundamental properties and behavior of domain structures needs to be translated into technological applications.

Conclusions

The properties of ferroelectric thin films are greatly influenced by their domain structure. As a result, control of the domain structure is vital to obtain desirable properties for technological applications. This paper has explored what parameters critically influence domain structures in ferroelectric thin films.

In doing so, both experimental and theoretical studies were examined to provide an understanding of both the breadth and depth of research in this field. Specific experimental studies highlighted how the different growth parameters influenced the domain structure. Fundamental knowledge of ferroelectric films has enabled the creation of powerful theoretical tools to further explore domain structures. Lastly, this paper highlighted research that must be done to continue to make meaningful progress in understanding and controlling ferroelectric domain structures.

Appendix A

Voigt Notation:

Voigt notation is a way to represent a systematic tensor by reducing its order. Using Voigt notation makes labeling easier as well as simplifying the representation of higher ranked tensors. In this notation the indices of the matrix elements are replaced by a single corresponding number. The specific substitutions are as follows for a symmetric second rank tensor; xx becomes 1, yy becomes 2, zz becomes 3, yz becomes 4, zx becomes 5, and xy becomes 6 [Dove]. The end result is that the 3x3 matrix has been reduced to a 6 dimension vector. The Voigt notation substitutions are illustrated in Figure 14.

$$\begin{pmatrix} \eta_{xx} & \eta_{xy} & \eta_{xz} \\ \eta_{yx} & \eta_{yy} & \eta_{yz} \\ \eta_{zx} & \eta_{zy} & \eta_{zz} \end{pmatrix} = \begin{pmatrix} \eta_1 & \eta_6 & \eta_5 \\ \eta_6 & \eta_2 & \eta_4 \\ \eta_5 & \eta_4 & \eta_3 \end{pmatrix} = (\eta_1 \quad \eta_2 \quad \eta_3 \quad \eta_4 \quad \eta_5 \quad \eta_6)$$

Figure 14. Voigt notation substitutions

References

[1] K. Lee, S. Baik, Annu. Rev. Mater. Res. 36, 81 (2006).

[2] Setter et al. J. Appl. Phys. 100, 051606 (2006).

[3] D.D. Fong, C. Thompson, Annu. Rev. Mater. Res. 36, 431 (2006).

[4] W. Pompe, X. Gong, Z. Suo, and J. S. Speck, J. Appl. Phys. 74, 6012 (1993).

[5] K. S. Lee, J. H. Choi, J. Y. Lee, and S. Baik, J. Appl. Phys. 90, 4095 (2001).

[6] J.S. Speck, W. Pomp , J. Appl. Phys. 76, 466 (1994).

[7]B.S. Kwak, A. Erbil , B.J. Wilkens, J.D. Budai, M.F. Chisholm, L.A. Boatner. Phys. Rev. Lett. 68, 3733 (1992)

[8] K. S. Lee and S. Baik, J. Appl. Phys. 87, 8035 (2000).

[9] Z. Li, C.M. Foster, D. Guo, H. Zhang, G.R. Bai, et al. Appl. Phys. Lett. 65, 1106 (1994)

[10] W. Y. Hsu, R. Raj, Appl. Phys. Lett. 67 792 (1995).

[11] A. L. Roytburd, Phys. Status Solidi A 37, 329 (1976).

[12] A. H. G. Vlooswijk, B. Noheda, G. Catalan, A. Janssens, B. Barcones, G. Rijnders, D. H. A. Blank, S. Venkatesan, B. Kooi, and J. T. M. de Hosson, Appl. Phys. Lett. 91, 112901 (2007).

[13] S. K. Streiffer, J. A. Eastman, D. D. Fong, C. Thompson, A. Munkholm, M. V. Ramana Murty, O. Auciello, G. R. Bai, and G. B. Stephenson, Phys. Rev. Lett. 89, 067601 (2002).

[14] C.M Foster, W. Pompe ,A.C. Daykin, J.S. Speck, J. Appl. Phys. 79, 1405 (1996).

[15] A. E. Romanov, W. Pompe, and J. S. Speck, J. Appl. Phys. 79, 4037 (1996).

[16] N. A. Pertsev and A. G. Zembilgotov, J. Appl. Phys. 78, 6170 (1995).

[17] O. Dieguez, S. Tinte, A. Antons, C. Bungaro, J. B. Neaton, K. M. Rabe, D. Vanderbilt, Phys. Rev. B 69, 212101 (2004).

[18] A. Kopal, B. Bahnik, J. Fousek, Ferroelectrics 202, 267 (1997).

[19] M. Dawber, K. M. Rabe, J. F. Scott, Reviews, Rev. Mod. Phys. 77, 1083 (2005).

[20] D. O. Klenov, T. R. Taylor, S. Stemmer, , J. Mater. Res. 19, 1477 (2004).

[21] B. Lai, I Ponomareva, I. Kornev, L. Bellaiche, and G. Salamo Appl. Phys. Lett. 91, 152909 (2007).

[22] W. Zhong, D. Vanderbilt, and K. M. Rabe Phys. Rev. B 52 6301 (1995)

[23] M. Dove, American Mineralogist 82, 213 (1997).

[24]W. Zhong, D. Vanderbilt, and K. M. Rabe, Phys. Rev. Lett. 73, 1861 (1994).

[25] L. Bellaiche, A. Garcı´a, and D. Vanderbilt, Phys. Rev. Lett. 84, 5427 (2000).

[26] I. Kornev, H. Fu, and L. Bellaiche, Phys. Rev. Lett. 93, 196104 (2004).

[27] A. Schilling, T. B. Adams, R. M. Bowman, J. M. Gregg, G. Catalan, J. F. Scott, Phys. Rev. B 74, 024115 (2006).

[28] M. Dove, Structure and Dynamics: An Atomic View of Materials (Oxford University Press, Oxford, 2003).